CHAPTER 3

Methodology

The RF-gun of the compact THz-FEL accelerator at Kyoto University produces free electrons via the photoelectric effect. Then, electrons are accelerated inside the standing-wave resonant cavities by the longitudinal electric field component of the radio-frequency (RF) wave. A solenoid magnet is placed downstream the RF-gun and is used for the electron beam focusing. To study properties of electron beams produced from the photocathode RF-gun, several diagnostic systems are used. The dipole magnet equipped with a view screen and CCD camera is utilized in the energy measurement. The quadrupole magnet and a view screen station are used to perform the beam emittance measurement via the quadrupole scan method. Contents in this chapter include the explanation about electron beam production and acceleration, the experimental set-ups, the measurement methods, and the analyses of the measurement results. The beam dynamic simulations were performed to compare the results with some experimental data. Thus, the simulation procedures are also described in this chapter.

3.1 Production of Photoelectrons

The RF-gun in this study consists of 1.6-cell standing-wave resonant cavities and a drive laser system. Free electrons are produced via the photoelectric effect from the photocathode, which is located at the center of the rear wall of the half-cell cavity. During this study period the copper cathode with a work function of around 4.5 eV was used. Electrons are emitted from the cathode, when the laser pulse with an energy higher than the cathode work function incidents the cathode surface.

The photocathode drive laser system consists of a mode-locked neodymium-doped yttrium orthovanadate (Nd:YVO_4) laser with acousto-optic modulators, two amplifiers, beam position stabilizers, a second harmonic generation (SHG) crystal and a fourth harmonic generation (FHG) crystal [35]. A typical emission wavelength of the Nd:YVO_4 laser is 1064 nm with a bandwidth of 1 nm [36]. The timing of the laser system is synchronized with the timing of the RF wave signal for efficient electron acceleration. In general, the laser operates in many oscillating modes. Interferences between the modes lead to random fluctuation in laser intensity. The mode-locked laser uses the acousto-optic modulator to fix the phase of each oscillating mode. Then, the light from each oscillating mode performs a periodic interference pattern and produces an intense laser pulse in a single mode. The acoustic-optic modulators (AOM) is, therefore, used to control power, frequency and spatial direction of the laser pulse by using an electrical drive signal [37]. A schematic diagram of the laser system for the photocathode RF-gun is shown in Fig. 3.1.

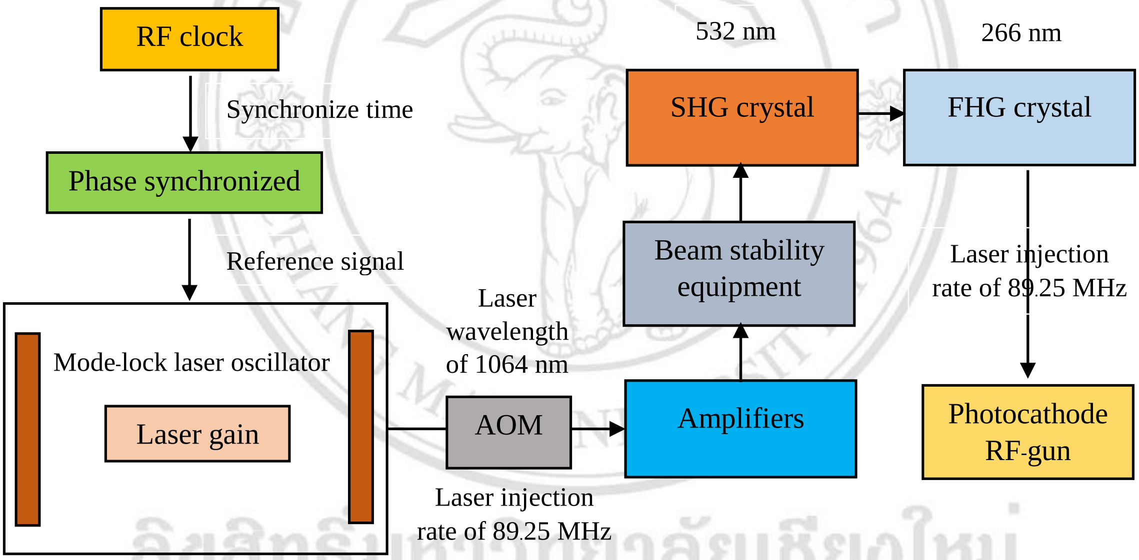

Figure 3.1: Schematic diagram of the drive laser system for the photocathode RF-gun.

The laser production process starts from generation of a low energy light pulse inside the master oscillator. In a resonant cavity of the master oscillator, the laser modes have wavelengths and frequencies, which are related to the boundary conditions as

$$\lambda_{n,res} = \frac{L}{2} \qquad \text{and} \qquad f_{n,res} = n\frac{c}{2L}, \tag{3.1}$$

where n is the integer numbers, which correspond to the number of wavelengths in a round trip in the laser cavity, c is the light velocity and L is the length of the resonant cavity. A series of 2-paths power amplifier is used to increase the laser pulse energy and the average power. In addition, optical equipments are inserted in the laser beam transport line to improve the light quality (such as a focusing condition), to display transverse and longitudinal laser beam profiles, to reduce the noise from the laser signal and to determine the micropulse structure. Then, the amplified laser pulses are injected to the nonlinear crystals, where the second harmonic generation (SHG) and the fourth harmonic generation (FHG) happen. The SHG is a coherent optical radiation process of the electric dipoles inside the potassium titanil phosphate ($KTiOPO_4$) non-linear crystal. If the electric field with a frequency of ω is applied to the crystal, the dipoles will oscillate and radiate the electric field with a frequency of 2ω [38]. The electric fields with frequencies of ω and 2ω have to be in phase, then the non-destructive interferences are formed. The concept of the SHG with the phase matching is shown in Fig. 3.2.

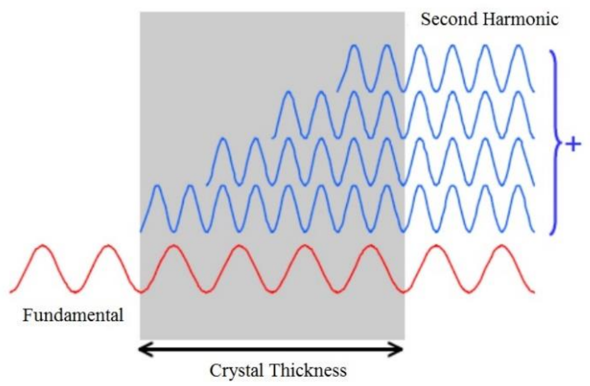

Figure 3.2: Simple figure shows the concept of the second harmonic generation (SHG) with the phase matching [38].

In this study, the laser with the fundamental wavelength of 1064 nm is converted to have the second harmonic wavelength of 532 nm. Then, it is converted to the fourth harmonic wavelength of 266 nm by using the potassium dideuterium phosphate (KDP) non-linear crystal. The final laser wavelength of 266 nm, which is in UV regime, has a pulse duration of 8 ps at FWHM [35]. The laser energy is then obtained by using the following equation

$$E_{laser} = h\nu = \frac{hc}{\lambda}, \tag{3.2}$$

where h is the Planck constant, ν is the laser frequency, c is the speed of light and λ is the laser wavelength. For the wavelength of 266 nm, the laser energy is calculated to be

4.66 eV, which is larger than the work function of the copper cathode of around 4.5 eV. The repetition rate of the injected laser is 89.25 MHz, which is defined by the mode-lock frequency of the laser oscillator. The phase synchronizer is used to synchronize the revolution time of the laser oscillator with the reference time of the RF wave signal. The phase of the laser oscillator (θ_{laser}) is obtained from

$$\theta_{laser} = \omega_{rf} t = 2\pi f_{rf} t\,, \tag{3.3}$$

where f_{rf} is the frequency of the RF wave and t is the revolution time of the injected laser. The electric field component of the RF wave at the cathode surface varies with time as shown in Fig. 3.3.

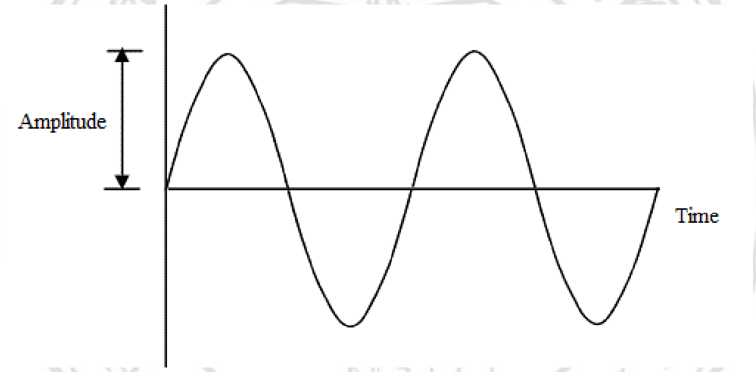

Figure 3.3: The time varying of the electric field at the cathode surface.

For acceleration of electrons with high efficiency, the laser injection phase is adjusted to generate electron pulses only in appropriate time, which must be related to the RF phase. Theoretically, the reference laser injection phase is defined as the phase when the electric field on the cathode surface is zero and it is called a zero-crossing or zero phase. In practice as in this study, the zero-crossing phase is assumed as the laser injection phase with no emitted electron from the RF-gun.

In principle, the energy of the emitted electrons from the cathode depends only on the energy of the incidence laser, while the laser intensity determines the number of emitted electrons. The diagnostic instruments for measuring the laser pulse energy are shown in Fig. 3.4. The properties of the photocathode drive laser for the electrons production are listed in Table 3.1.

Table 3.1: Properties of the photocathode drive laser for electron production.

Property	Value
Final laser wavelength	266 nm
Laser macropulse duration at FWHM	8 ps
RMS transverse size at FWHM	1.3 mm
Laser macropulse injection rate	89.25 MHz

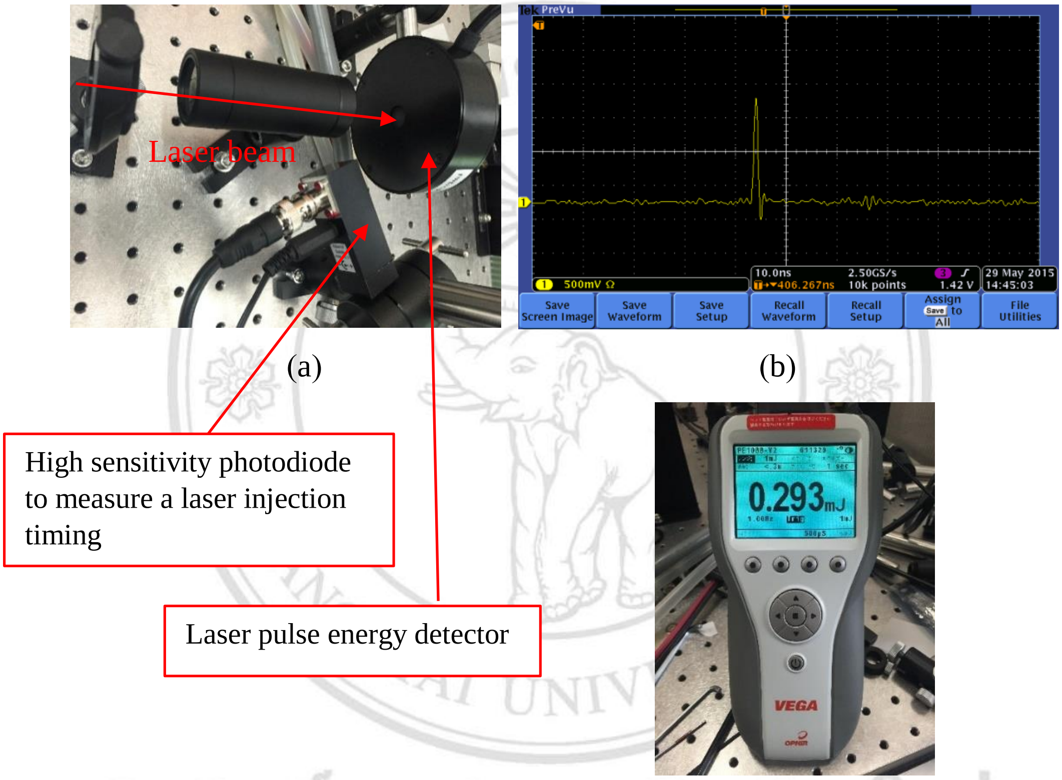

Figure 3.4: (a) Diagnostic instruments to measure the laser pulse energy and the laser injection timing. (b) Typical laser pulse for the timing measurement. (c) The laser pulse energy meter.

3.2 Acceleration of Electrons in RF-gun

3.2.1 Study of RF Wave Properties

In this study, the radio-frequency (RF) wave with a frequency of 2856 MHz is used to accelerate electrons inside the RF-gun. A high power RF wave is transported from a 10-MW klystron, through a rectangular waveguide system to an opening port at the radial wall of the full-cell cavity. Then, the wave is coupled to the half-cell cavity via the central iris between the two cavities. The RF wave in this study has a pulse duration of 2 µs with a macro-pulse repetition rate of 10 Hz. When the RF wave is transported into the RF-gun, the wave resonates inside the cavities and forms a standing-wave pattern in TM_{010}-mode. Some fraction of the RF wave is reflected back from the RF-gun. An RF circulator, which functions similar to a diode in an electric circuit, is installed downstream the klystron to protect it from the reflected wave. To measure both forward and reflected RF wave amplitudes, a directional coupler is installed between the RF-gun and the circulator. The signals from the directional coupler are used to study RF waveforms and to calculate a peak power of the forward and reflected RF waves. The RF waveform specifications and power are important parameters, which have the influence on the electron acceleration inside the RF-gun. To explain a mechanism of the RF acceleration in the RF-gun, an ideal rectangular RF waveform is introduced. For this particular waveform, each RF micropulse in the time domain of the macropulse has the same peak power. In this study, we consider the RF wave with a macropulse duration of 2 µs and a repetition rate of 10 Hz as shown in Fig. 3.5.

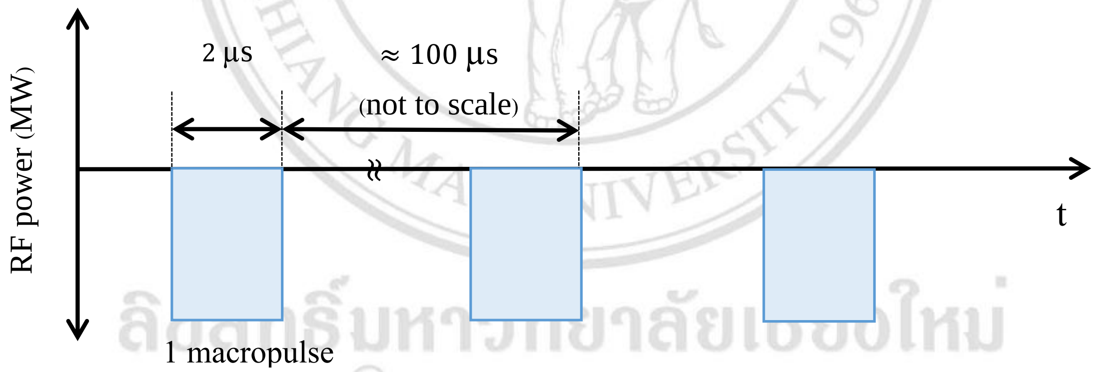

Figure 3.5: Schematic figure of ideal rectangular RF macropulses with the pulse duration of 2µs and the repetition rate of 10 Hz.

For the acceleration with 2-µs RF wave of 2,856 MHz at the repetition rate of 10 Hz, each macropulse contains 5,712 cycles of the RF wave. The time of the laser oscillator is synchronized with the reference time of the RF signal. Thus, the injection phase of the drive laser synchronizes with the appropriate phase of the RF wave. Since the frequency of the injected laser is 89.25 MHz, the laser pulses are injected 178.5 times in 2 µs. This results in the output electron macropulse of 178.5 microbunches. For the rectangular RF macropulse, all electron bunches are accelerated to exit the RF-gun with the same maximum kinetic energy and energy distribution. In practice, the RF generator cannot produce the RF wave with ideal rectangular macropulse waveform. There is a variation of the peak power within the RF macropulse and the micropulses in the time domain of the macropulse have different powers. Then, the microbunches of electron beam have different maximum kinetic energies and energy distributions.

The RF wave signals from the directional coupler are detected by using crystal detectors, which transform the RF signal to DC voltage. To protect the damage of the RF crystal detectors, some attenuators are used to reduce the amplitude of the RF wave. A logarithmic scale of the relative RF power after the attenuation is obtained from

$$P(dB) = 10\log(P / \mathrm{P}_{ref}), \tag{3.4}$$

where P is the measured RF power with the attenuation and P_{ref} is the reference RF power. When the reference power is 1 mW, the relative RF power is

$$P(dBm) = 10\log(P[mW]/1[mW]). \tag{3.5}$$

Thus, the measured RF power with the attenuation becomes

$$P_f[mW] = 10^{(P(dBm)/10)}. \tag{3.6}$$

For this research, a calibration between the measurement voltage obtained from the oscilloscope and the crystal detector measurement power is shown in the following equation

$$P[mW] = 0.12609 + 0.0375V + 0.00127V^2, \tag{3.7}$$

where V is the measured RF voltage in unit of mV. A total attenuation of the measurement system, which includes the cable, the crystal detector and the oscilloscope, is 82.5 dBm. Therefore, the forward RF power can be obtained by using the following calibration equation

$$P_f[MW] = 10^{-9} \times 10^{((10\cdot\log(0.12609+0.0375\cdot V+0.00127\cdot V^2)+82.5)/10)}, \tag{3.8}$$

An example of the actual RF signals of the macropulse duration of 2 μs, which was measured by the oscilloscope, is shown in Fig. 3.6. A measured voltage of the forward

RF wave in Fig. 3.6 is 184.4 mV, which is calculated to be the RF peak power of 8.93 MW. The relationship between the forward RF power and the measured voltages are shown in Fig. 3.7. Properties of the RF wave for the electron acceleration in this study are listed in Table 3.2.

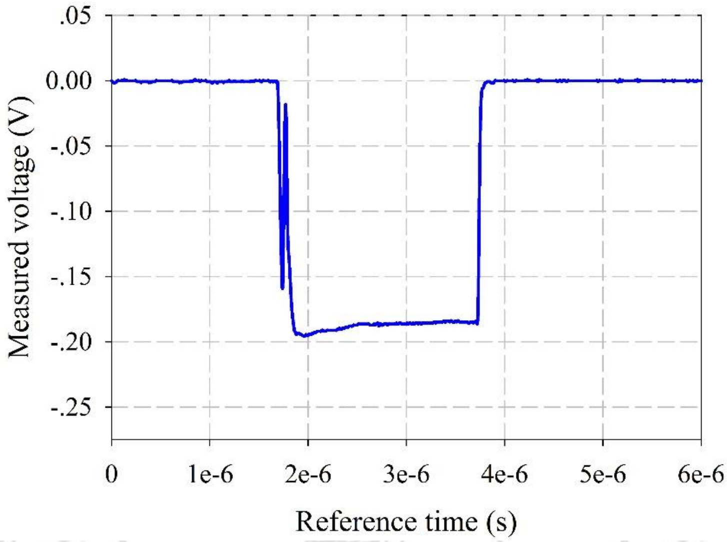

Figure 3.6: Measured forward RF signal for the RF pulse width of 2 μs.

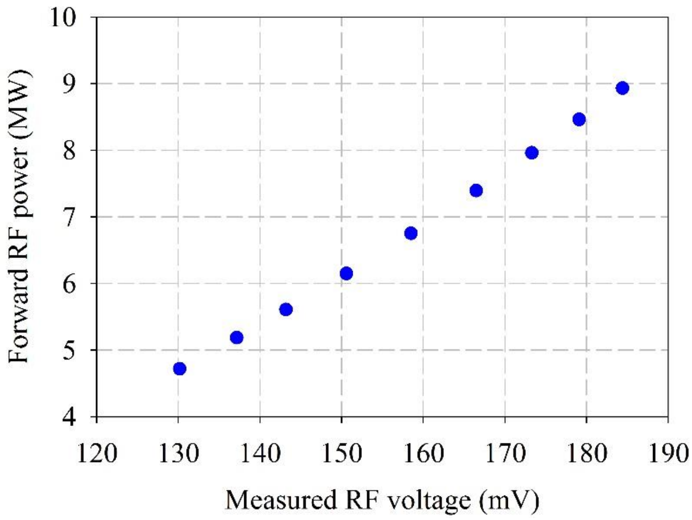

Figure 3.7: Forward RF power as a function of the measured RF voltage.

Table 3.2: Properties of the RF wave for electron acceleration in this study.

Property	Value
RF frequency	2,856 MHz
Macropulse duration	2 μs
Macropulse repetition rate	10 Hz
RF peak power	5 – 9 MW

3.2.2 Simulations of Electromagnetic Field Distribution in the RF-gun

The photocathode RF-gun in this study has two resonant cavities, a half-cell and a full-cell. Two-dimensional electromagnetic field simulation was performed by using the program SUPERFISH [39]. This program was used to create the cylindrical symmetric electromagnetic (EM) field distribution of the RF cavity. The program solves the EM field from the differential form of Maxell's equations. Dimensions the of RF cavity in longitudinal and radial directions are used in the boundary conditions of the program. A triangle mesh is introduced for calculation of the coordinates of the interior points. Then, the tridiagonal method is used to solve the EM field in each point inside the boundary condition [40].

Results from SUPERFISH simulations show that the effective lengths of the half-cell and the full-cell are 2.549 cm and 3.989 cm, respectively. Simulated electric field profiles inside the half-cell and the full-cell cavities are shown in Fig. 3.8. The horizontal axis and the vertical axis of the plots refer to the longitudinal axis and the radial axis of the RF-gun. As shown in the figure, the longitudinal electric field (E_z) is maximum at r = 0 and it reduces gradually when the cavity radius increases. According to the design properties, the RF-gun will be operated with an average accelerating gradient of about 50 MV/m to reach a maximum kinetic energy of about 4.5 MeV at the RF-gun exit. 2D-normalized simulated electric field profiles inside the two cavities are shown together with the simulated longitudinal solenoid magnetic field profile in Fig. 3.9.

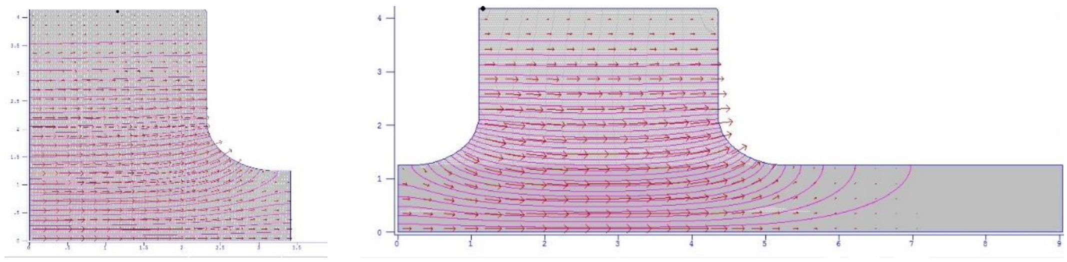

(a) (b)

Figure 3.8: Simulated electric field profiles inside (a) the half-cell and (b) the full-cell cavities.

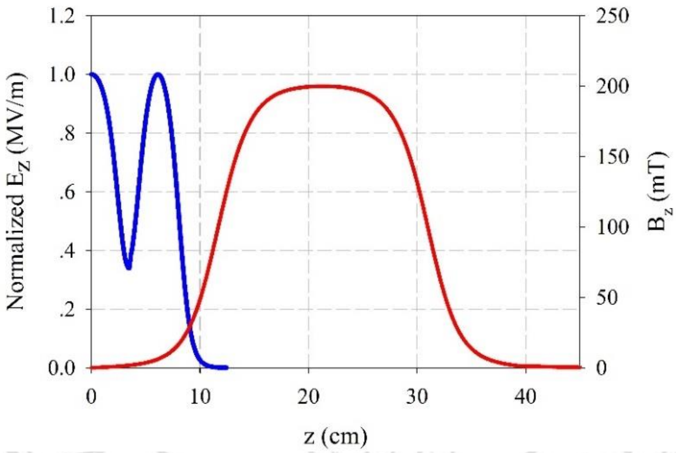

Figure 3.9: Distributions of the normalized longitudinal electric field (E_z) and the longitudinal magnetic field (B_z) at r = 0 inside the half-cell and the full-cell cavities.

In this study, the position of the photocathode is used as the longitudinal reference position (z = 0). The half-cell and the full-cell cavities occupy the space from the positions z = 0 to z = 3.4135 cm and z = 3.4135 to z = 12.454 cm, respectively. The center of the solenoid field is at z = 22 cm and its magnetic field distribution starts from z = 0 to z = 50 cm. The design maximum magnetic field of the solenoid magnet is 200 mT.

3.2.3 Beam Dynamic Simulations

Beam dynamic simulations were performed in order to investigate the properties of electron beams produced from the photocathode RF-gun. The considered properties are electron bunch charge, electron beam energy, transverse beam size and transverse beam emittance. The main components included in the simulations are the RF-gun and the focusing solenoid magnet. The electromagnetic field distributions obtained from SUPERFISH simulations are included in the beam dynamic simulations with the program

PARMELA [10]. This program tracks the particles through the EM field and calculates 6-dimensional coordinates $(x, x', y, y', E, \varphi)$ of the particles at each position, which corresponds to the calculation step size (mesh) and the boundary condition. The program PARMELA can simulate transverse and longitudinal motions of electrons when they travel through the electric and magnetic field distributions inside the RF-gun, the solenoid magnet and other elements in the beam transport line. In this study, it performs a single bunch calculation, which includes the effect of image charges in the conducting wall of the accelerator and the 2D space charge effect.

For all simulations in this thesis the initial particle distributions at the cathode (z = 0) is created by using the laser parameters as shown in Table 3.3. The transverse and longitudinal particle distributions at cathode are shown in Fig.3.10.

Table 3.3: Simulated parameters used in PARMELA simulations.

Parameter	Value
Laser spot size at FWHM	1.378 mm
Laser pulse length at FWHM	8 ps
Initial energy at cathode	10 eV
Electron bunch charge	50 pC

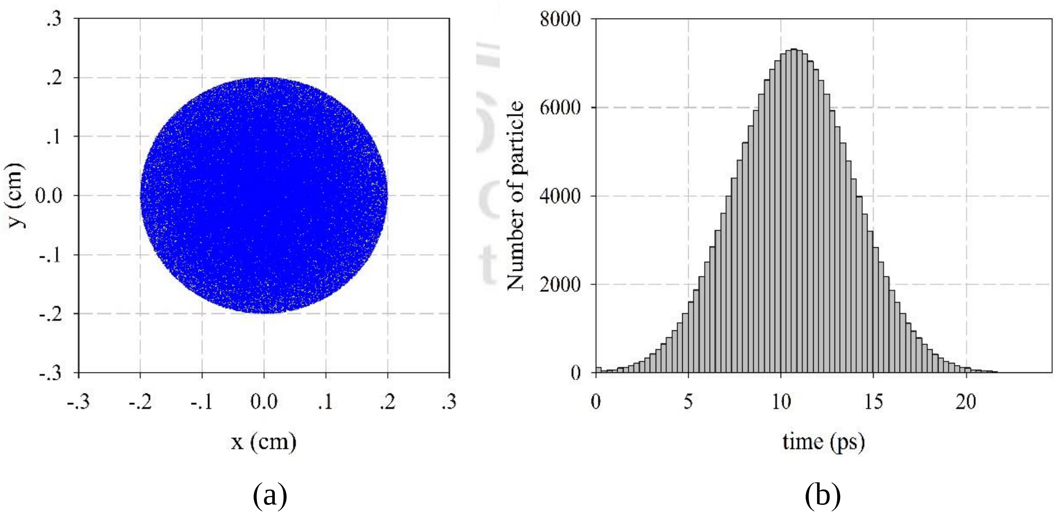

Figure 3.10: (a) Transverse and (b) longitudinal distributions of the initial electron bunch at the cathode (z = 0).

In order to perform the beam dynamic simulations with acceptable accuracy results, optimizations of particle numbers and mesh sizes in both radial and longitudinal directions were conducted. In PARMELA simulations, we assume that groups of electron called "macro-particles" are emitted from the photocathode with Gaussian distribution in both transverse and longitudinal axes. In the optimization of the number of macro-particles, mesh sizes in radial and longitudinal direction of 0.4 mm and 0.575 mm were used, respectively. The dependence of electron energy, transverse beam size and beam emittance on the number of macro-particles was investigated. The maximum and average electron energy dependences on the number of macro-particles are shown in Fig. 3.11. The RMS transverse beam size and emittance in x-axis and y-axis as a function of the number of macro-particles are shown in Fig. 3.12. The simulation results in the Fig. 3.11 and 3.12 show that all considered parameters mentioned above converse to constant values when the number of macro-particles is larger than 200,000 particles. Thus, the optimal number of macro-particles, which was used in all following simulations, was chosen to be 200,000. In the optimization procedure, all macro-particles represent the total bunch charge of 50 pC. Thus, each macro-particle has the charge of 250 aC (atto-Coulomb) or 1557 electrons.

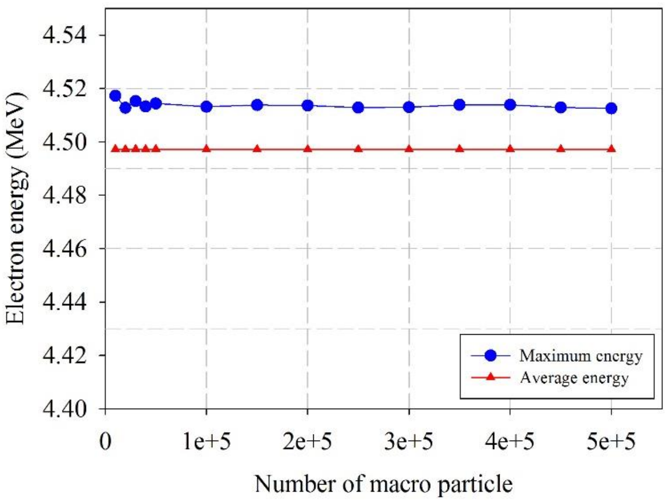

Figure 3.11: Relationship between the number of macro-particles and the simulated maximum and average electron energies.

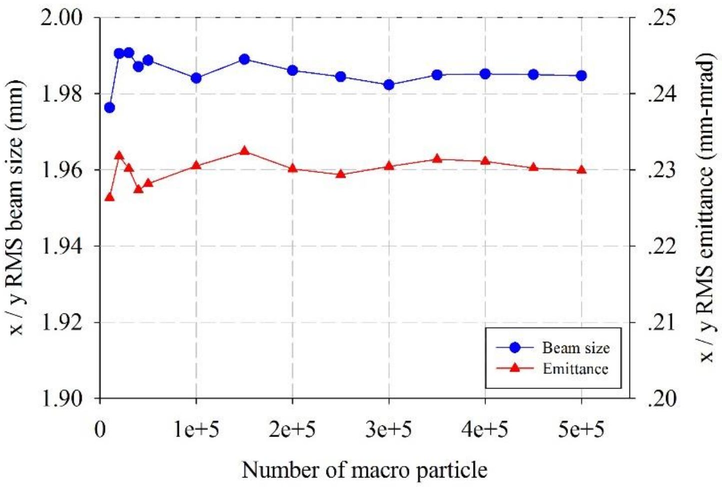

Figure 3.12: RMS transverse beam size and beam emittance in x-axis and y-axis as a function of the number of macro-particle.

In optimization of the radial and longitudinal mesh sizes, the optimal number of macro-particles of 200,000 particles was used. Firstly, the radial mesh size was varied while the longitudinal mesh size was kept at 0.575 mm. The results of this optimization are shown in Fig. 3.13 and Fig. 3.14. The values of maximum and average electron energies as well as the RMS transverse beam size and the beam emittance converse to constant values when the radial mesh size is smaller than 0.25 mm. Thus, an appropriate radial mesh size, which was used in all following simulations, is 0.25 mm.

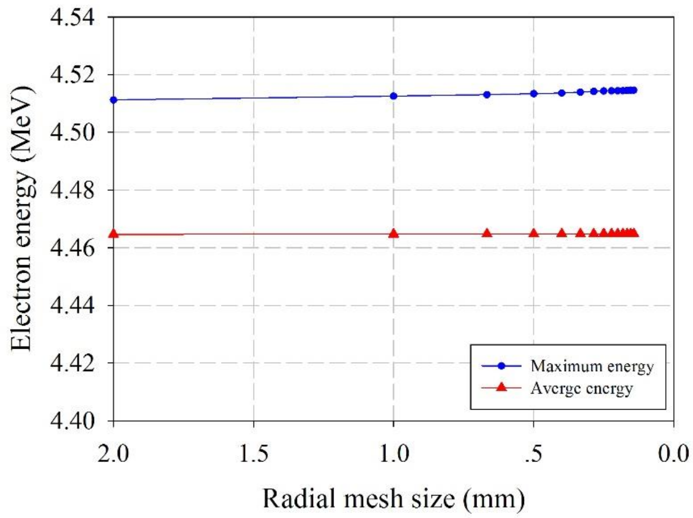

Figure 3.13: Relationship between the maximum and average electron energies and the radial mesh size.

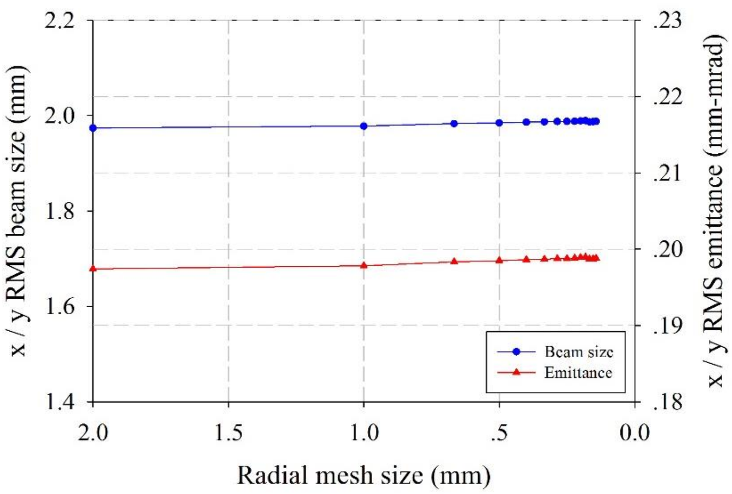

Figure 3.14: Relationship between the RMS transverse beam size and emittance in x and y axes and the radial mesh size.

In the optimization of the longitudinal mesh size, the radial mesh size was set to the optimal value of 0.25 mm. The optimization results in Fig. 3.15 and 3.16 show that the maximum and average electron energies, the RMS transverse beam size and the beam emittance are almost constant when the longitudinal mesh size is smaller than 0.575mm. Therefore, the optimal radial and longitudinal mesh sizes, which were used in all simulations in this thesis are 0.25 mm and 0.575 mm, respectively.

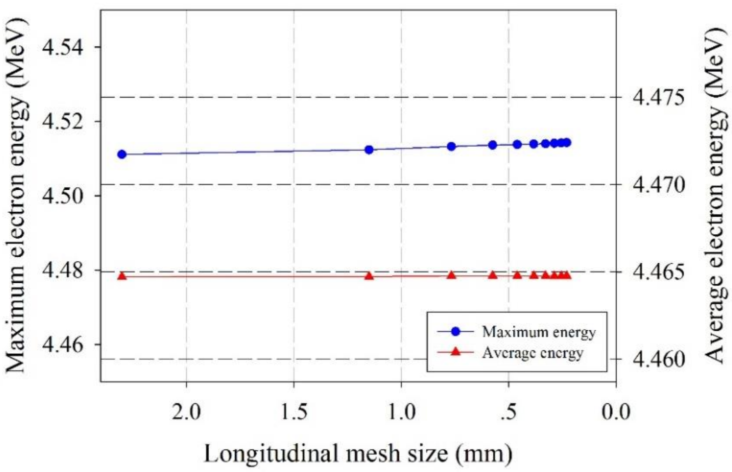

Figure 3.15: Relationship between the maximum and average electron energies and the longitudinal mesh size.

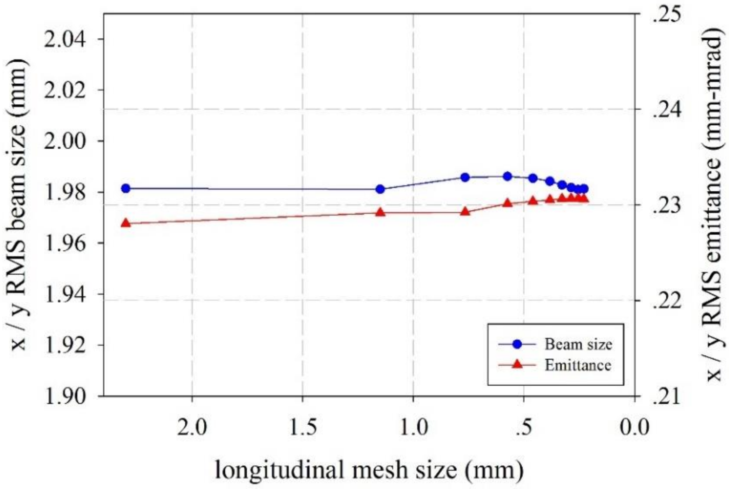

Figure 3.16: Relationship between the RMS transverse beam size and beam emittance in x and y axes and the longitudinal mesh size.

By using all optimal parameters obtained from the optimizations and the laser injection phase of 10 degree, examples of the transverse distribution and transverse phase spaces of an electron bunch at the end of the solenoid magnetic field (z = 50 cm) are shown in Fig. 3.17 and Fig. 3.18, respectively. For these examples, the accelerating gradient of 50 MV/m, the bunch charge of 50 pC and the solenoid magnetic field of 200 mT were used. The longitudinal phase space (E vs. t) at the position of z = 50 cm is also shown in Fig. 3.19.

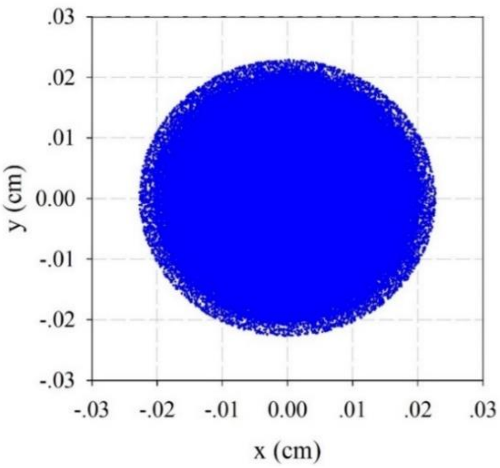

Figure 3.17: Example of transverse distribution in x-y plane of the electron bunch at the position of z = 50 cm.

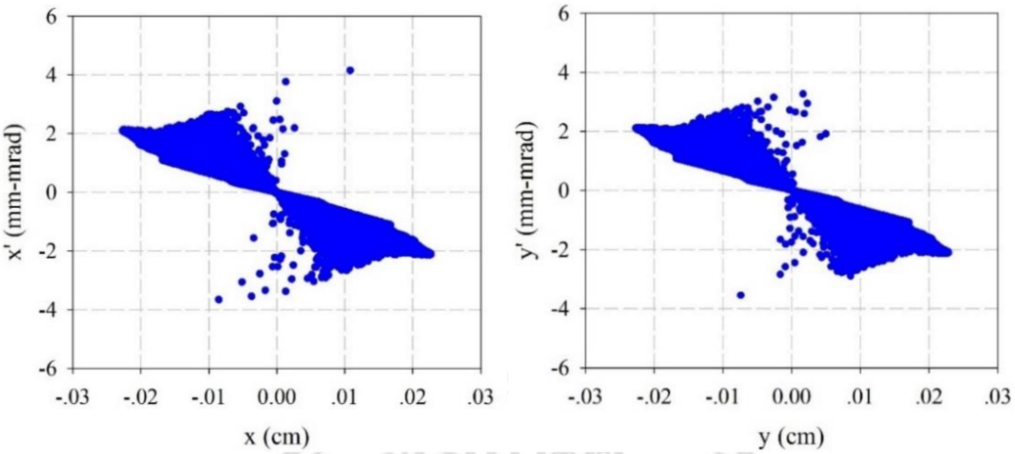

Figure 3.18: Examples of transverse phase spaces ($x-x'$) and ($y-y'$) of the electron bunch at the position of z = 50 cm. The RMS transverse emittance is calculated to be 0.02 mm-mrad.

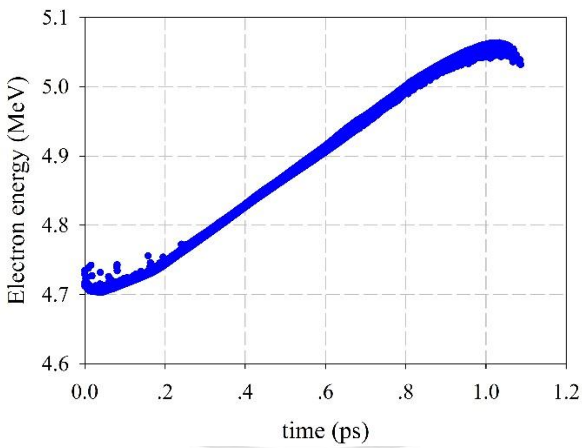

Figure 3.19: Relationship between the electron energy and the longitudinal position of the simulated electron beam at the position z = 50 cm.

As shown in Fig. 3.19, the low energy electrons are located at the head of the bunch and the high energy electrons are located at the tail of the bunch. This distribution is suitable for the bunch compression with the chicane magnetic bunch compressor, which consists of four dipole magnets, to reduce the longitudinal bunch length. In this case, the low energy electrons enter the bunch compressor before the high energy electrons and their travel paths inside the bunch compressor are larger than the high energy ones. Thus, the longitudinal bunch length decreases when the beam exits the bunch compressor.

3.2.4 Estimation of Cavity Wall Loss Power

Inside the RF-gun, some fraction of the RF wave penetrates into the cavity wall (P_{cy}) and some fraction is used to accelerate electrons inside the RF-gun (P_b). A relationship between the forward RF power (P_f), the reflected RF power (P_{re}), the cavity wall loss power (P_{cy}) and the beam power (P_b) can be written as

$$P_f = P_{re} + P_{cy} + P_b . \tag{3.9}$$

Consider the case of no emitted electron from the cathode, the relationship of the RF powers in equation (3.9) becomes

$$P_f = P_{re} + P_{cy} . \tag{3.10}$$

The relationship between the accelerating voltage (V_{acc}) and the cavity wall-loss power (P_{cy}) as explained in Chapter 2 is written as

$$P_{cy} = \frac{V_{acc}^2}{r_s d} = \frac{E^2 d}{r_s} , \tag{3.11}$$

where E is the average accelerating gradient, d is the effective length of the resonant cavity and r_s is the shunt impedance per unit length of the cavity. Since the RF-gun has two cavities, then equation (3.11) becomes

$$P_{cy} = \frac{E_1^2 d_1}{r_{s1}} + \frac{E_2^2 d_2}{r_{s2}} . \tag{3.12}$$

where the effective lengths d_1 and d_2 are 2.549 and 3.989 cm, respectively. The shunt impedance per unit length r_{s1} and r_{s2}, obtained from SUPERFISH simulations are 109.947 MΩ/m and 48.948 MΩ/m, respectively. In case of the accelerating gradients E_1 and E_2 of 50 MV/m, the cavity wall-loss is

$$P_{cy} = \frac{50^2[MV/m]^2 \times 0.02549[m]}{109.947[M\Omega/m]} + \frac{50^2[MV/m]^2 \times 0.03989[m]}{48.948[M\Omega/m]} = 2.6\, MW .$$

3.3 Electron Beam Focusing

For the KU compact THz-FEL accelerator, a solenoid magnet is installed around a vacuum chamber downstream the RF-gun for electron beam focusing. The solenoid magnet consists of pancake coils made of square copper tubes with a central hollow. The iron plates are inserted between the pancake coils. Then, the coils and the iron plates are stacked and clamped together to form the solenoid structure. The entire solenoid magnet is covered with a metal chamber for straighten the magnetic flux in order to achieve more uniform magnetic field. However, the iron plates at the entrance and the exit ends of the solenoid magnet are thin and a fringe field is exhibited. The fringe field has radial components, which are used to focus the electron beam. A water cooling system is connected to the magnetic coils for removing the heat. A photograph of the entire solenoid magnet and a pancake coil are shown in Fig. 3.20. The solenoid magnetic field was measured with the experimental setup shown in Fig. 3.21. The setup consists of a 40 V/200 A power supply, a 3-D magnetic probe, a 1-D translation state, and switches for safety stop of the translation state. Four thermometer sensors are installed on the outer wall of the solenoid magnet chamber and are directly connected to the control system. Then, the power supply can be shut down if the solenoid magnet is over heat.

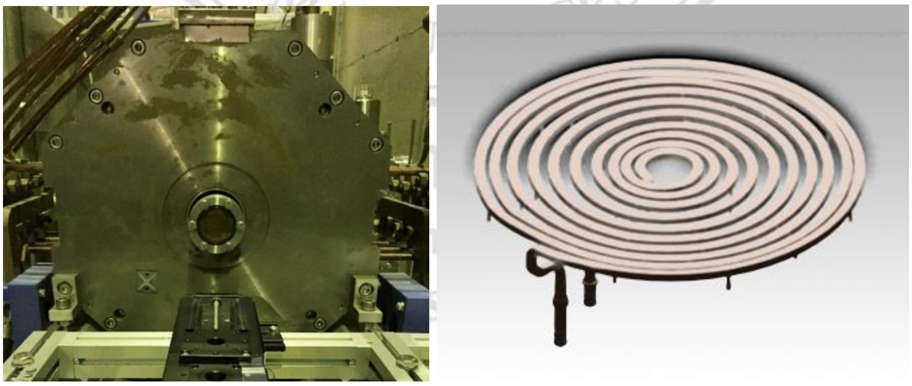

(a) (b)

Figure 3.20: Photographs of (a) the solenoid magnet and (b) the pancake coil [41].

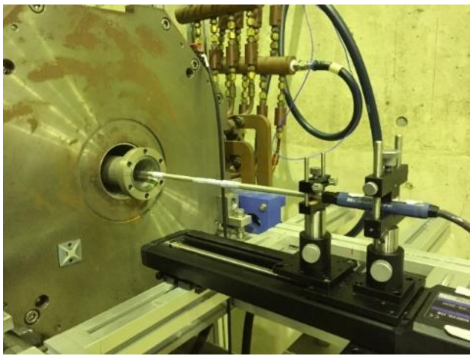

(A)

(B) (C)

Figure 3.21: (A) Experimental set-up of the magnetic probe on the translation state.
(B) Thermometer and one of sensors on the outer wall of the solenoid chamber.
(C) The 40 V/200 A power supply, which was used in the magnetic field measurement of the solenoid magnet.

The longitudinal magnitude field component (B_z) along z-axis of the solenoid magnet was measured by using an applied current of 100 A. The values of the longitudinal magnetic field B_z as a function of the distance in z-axis are shown in Fig. 3.22. The simulated magnetic field (blue line) and the measured magnetic field (red dots) show similar field distributions. Both simulated and measured fields are symmetry along the z-axis. Maximum values of the solenoid field at the center of the z-axis are 148.65 mT and 148.66 mT for the simulation and the measurement results, respectively. The magnitude of B_z along z-axis is maximum and almost constant at the positions near the center of the magnet in both positive and negative directions (±2 cm). Moreover, the relationship of the longitudinal magnetic field and the applied currents from zero to 200 A with a step of 10 A are shown in Fig. 3.23.

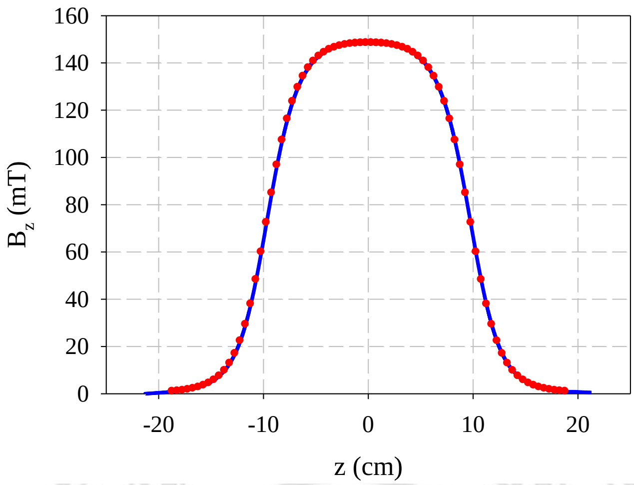

Figure 3.22: Simulated (blue line) and measured (red dots) solenoid longitudinal fields as a function of the distance in z-axis.

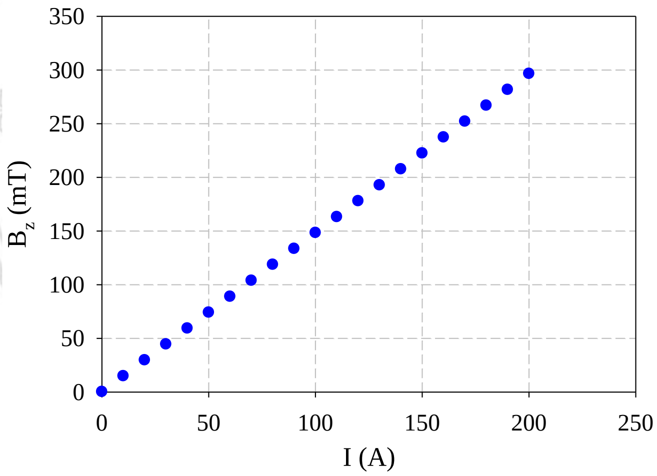

Figure 3.23: Measured longitudinal magnetic field (B_z) as a function of the applied current (I).

The relationship in Fig. 3.23 show a linear correlation between the magnetic field B_z and the applied current. The magnitude of the magnetic field is around 300 mT for the maximum applied current of 200 A. The fitting equation of the graph in Fig. 3.23 can be written as

$$B_z[mT] = 1.4822 \cdot I[A] + 0.108\,, \tag{3.14}$$

where B_z is the longitudinal magnetic field magnitude and I is the applied current. Examples of the longitudinal solenoid magnetic field and the integration of the field along the z-axis when using the applied current of 100 A are shown together in Fig. 3.24. The effective length (l_{eff}) of the solenoid magnet is calculated from

$$l_{eff} = \frac{\int B_z dz}{B_z(0,0,0)}, \tag{3.15}$$

where $B_z(0,0,0)$ is the value of B_z at the center of the solenoid magnet, which equals to 148.66 mT, and the value of the longitudinal field integration along the z-axis is 2886.14 mT-cm. Therefore, the effective length of the dipole magnet is calculated to be 19.41 cm. Information of the measured and simulated magnetic fields of the solenoid magnet are used in optimization of the electron beam transverse properties, which is described in Chapter 4.

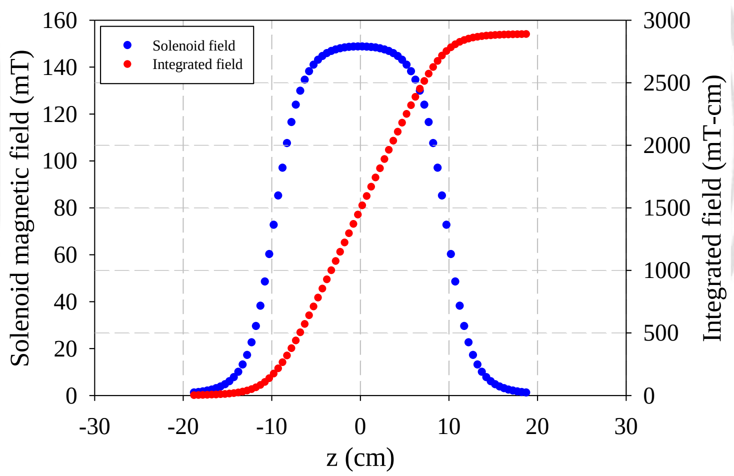

Figure 3.24: Measured longitudinal solenoid magnetic field and the integration of the field along z-axis.

3.4 Electron Bunch Charge Measurement

In this study, a Faraday cup is used to measure the dark current and the electron bunch charge. Generally, the Faraday cup is used to measure a macrobunch charge. However, for this study, it can be used to measure the microbunch charge because a spacing in time domain of each microbunch is long enough, which corresponds to the laser injection rate of 89.25 MHz. The measurement system consists of a Faraday cup, a coaxial cable and an oscilloscope. The Faraday cup in this study is made of graphite and the bunch charge measurements were performed in air. The extraction window is placed at the end of a view screen vacuum chamber to keep a vacuum condition inside the accelerator system. In principle, when electrons impact on the Faraday cup surface, secondary electrons are emitted. The theory suggests that the secondary electron emission occurs in three steps [42]. Firstly, the primary electrons hit electrons at the Faraday cup surface and transfer the kinetic energy to produce internal secondary electrons. Secondly, internal secondary electrons travel through the Faraday cup material towards the surface. Lastly, the secondary electrons escape from the material surface. The secondary electrons are then observed as the electrical signal on the oscilloscope. In case of high average electron current, a water cooling system may be needed to control the temperature of the Faraday cup. The view screen station equipped with the CCD camera system is used to monitor the transverse size and the position of the electron beam before it exits the extraction window. This is in order to ensure that the beam will hit the center of the Faraday cup. A photograph and a layout of the experimental set-up for the charge measurement is shown in Fig. 3.25 and Fig. 3.26, respectively.

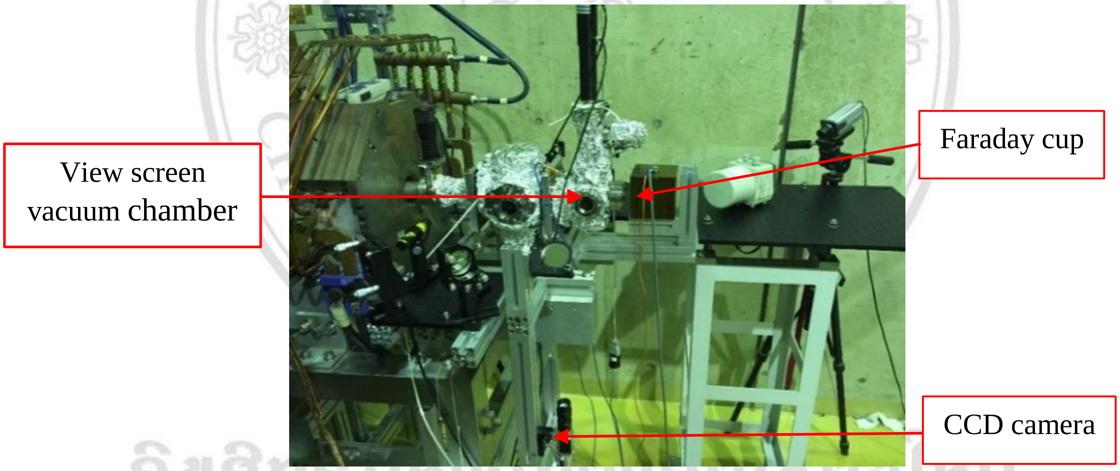

Figure 3.25: Photograph of the experimental set-up for the charge measurement.

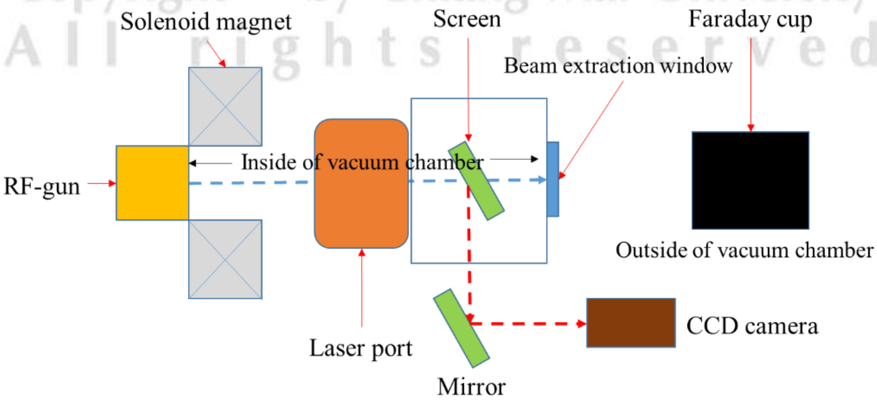

Figure 3.26: Layout of the experimental set-up for the charge measurement.

The extraction window made of copper with a thickness of 0.2 mm and the density of 8.96 g/cm^3. For the electron beam with an average energy of around 4.5 MeV, the collision stopping power is 1.346 MeV-cm^2/g and the radiative stopping power is 0.2261 MeV-cm^2/g [43]. Thus, the total stopping power of the copper window for the 4.5 MeV electron beam is 1.573 MeV cm^2/g. The energy loss of electrons at the window is obtained from

$$E_{loss} = S_{tot}(E)\rho d \ , \tag{3.16}$$

where $S_{tot}(E)$ is the total stopping power of the electrons at the copper window, ρ is the density of the copper window and d is the thickness of the copper window. In this case, the energy loss is calculated to be 282 keV. The electron beam exiting from the copper window travels in air for 1 cm and hits the surface of the Faraday cup. The procedure of the charge measurement is discussed as following:

(1). The experimental set-up was assembled such that the Faraday cup is electrically separated from other components in the beam transport line. Then, the cup is connected to an oscilloscope via a coaxial cable. Calibration of the observed signal on the oscilloscope was done to ensure the precision of the measurement data.

(2). The dark current was measured when the laser was turned off. The dark current comes from the field emission effect of the RF wave with a high electric field strength. This current is related to the power of the RF wave inside the RF-gun, which is given by

$$I(t) = \frac{V(t)}{R} \ , \tag{3.17}$$

where $V(t)$ is the measured voltage monitored by the oscilloscope and R is the resistance of the measurement system. Then, the charge of the dark current, which is the background charge, is obtained from the following equation

$$Q = \int I(t)dt = \frac{1}{R}\int V(t)dt \ . \tag{3.18}$$

(3). The total electron beam current was measured when the laser was turned on. Then, the values of electron current and charge are obtained by using the same formulas in equations (3.17) and (3.18). Finally, the actual electron bunch charge is calculated by subtracting the total electron charge with the charge of the dark current.

3.5 Measurement of Electron Beam Energy

The set-up for the beam energy measurement consists of a dipole magnet, a fluorescence screen, and a CCD camera system. A photograph of the experimental set-up is shown in Fig. 3.27. All energy measurements presented in this thesis were performed outside the vacuum chamber. A Mylar window is used to close the end of the vacuum chamber and lets the electron beam to pass with small energy loss. It is made of 0.1 µm aluminum sheet with polyimide coated surface of 0.3 µm thick [44]. Therefore, the total thickness of the Mylar window is 0.4µm. Since the total stopping power of the aluminum is 1.664 MeV-cm^2/g for the electron energy of 4.5 MeV [43] and the density of the aluminum of 2.70 g/cm^3, the energy loss when the electron beam passing through the aluminum sheet can be calculated by using the equation (3.16) and the result is 44.93 eV.

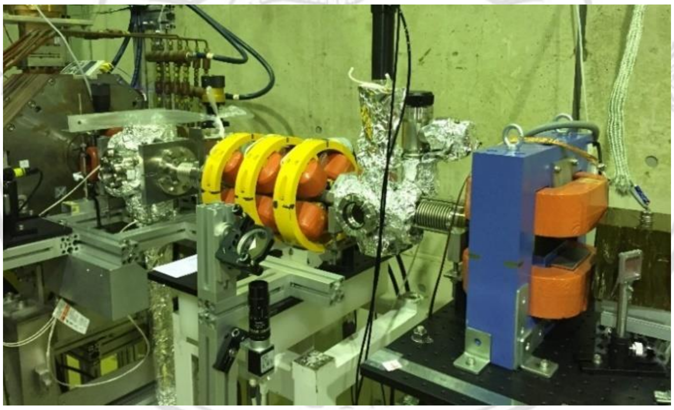

Figure 3.27: Photograph of the experimental set-up for the beam energy measurement.

For the polyimide coated layer, the density and the stopping power of the polyimide are 1.42 g/cm^3 and 1.82 MeV cm^2/g, respectively [45]. The energy loss when the electron beam passing through the 0.3 µm thick polyimide layer is calculated to be 77.53 eV. Then, the energy loss due to both aluminum sheet and polymide coated layer is 122.46 eV, which is very small compared to the electron beam energy of around 4.5 MeV. In addition, the density of the air inside the accelerator room is 1.20×10^{-3} g/cm^3 and the electron stopping power in the dry air is around 1.881 MeV cm^2/g for the 4.5 MeV electron [43]. The energy loss of electrons in air is calculated to be 2.257 keV per 1 cm. Since the total path length from the Mylar window to the view screen downstream the dipole magnet is about 25.6 cm, the energy loss of electrons in air is about 57.78 keV.

Thus, there is a small change (about 1.3%) of the electron energy when the beam passes through the Mylar window and the air before it hits the view screen. Although, the Mylar window is very thin, it can stand for a vacuum pressure of about 6.5×10^{-3} Pa without damage. After exiting the Mylar window, the electron beam travels through the magnetic field of the dipole magnet, which bends the electron path to hit the fluorescence screen as shown in Fig. 3.28. In this set-up, the dipole magnet with a pole length of 6.5 cm and an effective length is 10.6 cm is used. The distances from the magnet to the screen in z-axis and in x-axis are 10 cm and 6 cm, respectively.

When the beam travelling along a dispersive region of the dipole magnet, the bending radius of electron traveling path is related to the total beam energy (E) as

$$\frac{1}{\rho[m]} = \frac{0.2998 B_0 [Tesla]}{\beta E_{total} [GeV]}, \tag{3.19}$$

where B_0 is the peak magnetic field of the dipole magnet, β is the electron velocity in term of velocity of light $(\beta = v/c)$ and ρ is the curvature radius of the electron traveling path. Therefore, electrons with different energies bend in the dispersive region of the dipole magnet with different bending radii. A CCD camera is used to observe and record a transverse beam distribution on the fluorescence screen downstream the dipole magnet. An image of the screen captured by the CCD camera is shown in Fig. 3.29.

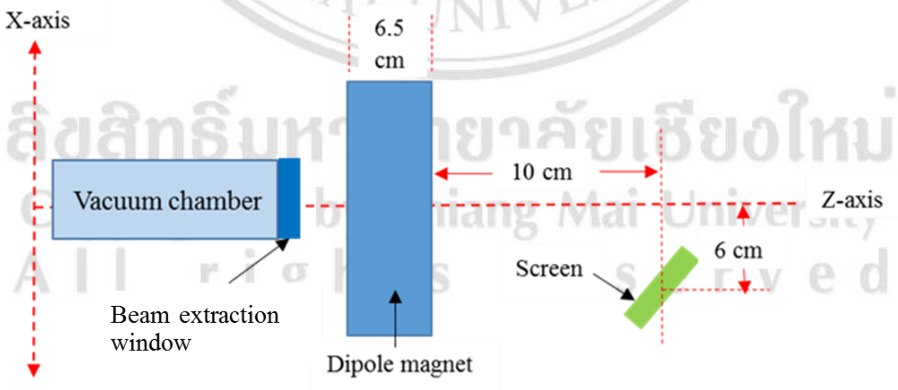

Figure 3.28: Layout of the experimental set-up for the beam energy measurement.

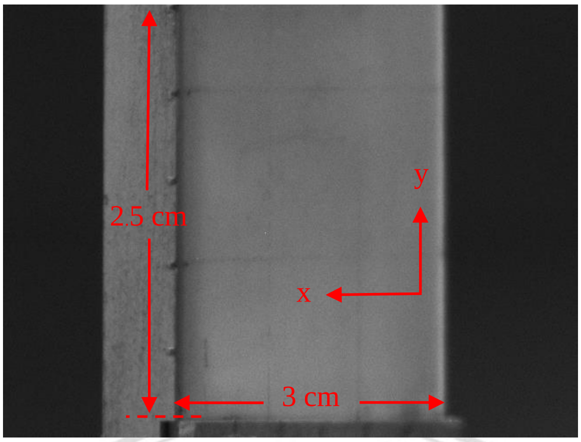

Figure 3.29: Image of the fluorescence screen with dimensions for the measurement of electron beam energy.

The CCD camera captures the image with the image sizes in x-axis and y-axis of 510 and 500 pixels, respectively. According to the screen dimensions as shown in Fig. 3.29, the screen sizes are 3 cm in x-axis and 2.5 cm in y-axis. Thus, the image resolutions for x-axis and y-axis are 58 and 50 μm/pixel, respectively. These resolutions are then used to study the distributions of the incident electrons on the screen in order to determine the beam energy.

The dipole magnet, which was used to measure the electron beam energy in this study is one of the dipole magnets in the chicane system, which the completed system will be installed later in the accelerator system. It is an electromagnet with a maximum magnetic field of around 300 mT when using an applied current of 20 A. It has a physical yoke width of 6.5 cm, a pole face width of 10 cm and a pole gap of 28 mm. The conducting coil has 190 turns. A photograph of the dipole magnet is shown in Fig. 3.30. According to the coil structure and the applied current direction, induced magnetic field lines point from the upper pole to the lower pole. Therefore, the electron beam bends in x-axis when it travels in the gap between the poles of the magnet.

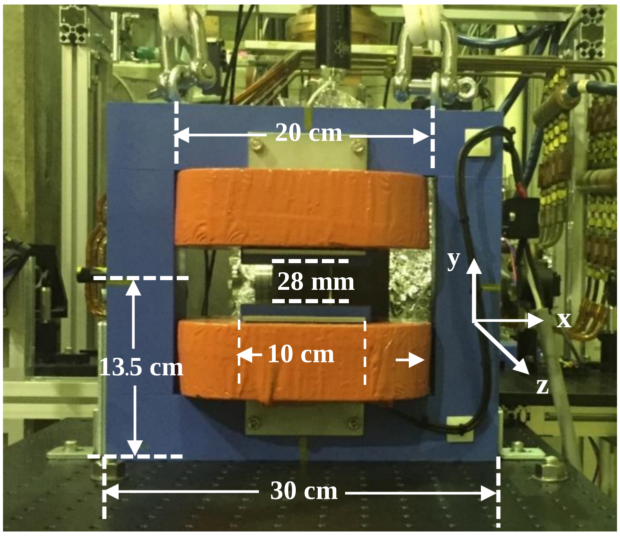

Figure 3.30: Photograph of the dipole magnet used in electron beam energy measurements.

A 3-dimensional translation state, a magnetic probe, a control system, and a power supply (as shown in Fig. 3.31.) are used to measure longitudinal and transverse components of the dipole magnetic field. Movement lengths of the magnetic probe in x, y and z axes are 18.5, 8.0 and 2.2 cm, respectively. Steps of the movements in x, y and z axes are 0.5, 0.2 and 0.1 cm.

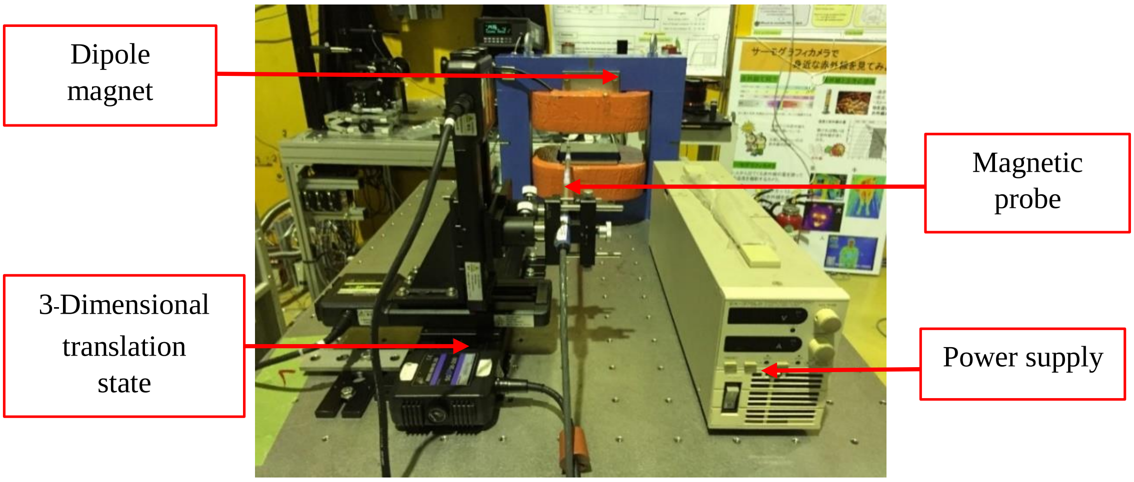

Figure 3.31: The experimental set-up for the dipole magnetic field measurements.

In the measurement of the magnetic field distribution, an applied current of 10 A was used. Numerical simulations of the magnetic field distribution were performed by using the RADIA program [46]. A comparison between simulation and measurement results of the vertical magnetic field component (B_y) along the z-axis of the dipole magnet is shown in Fig. 3.32.

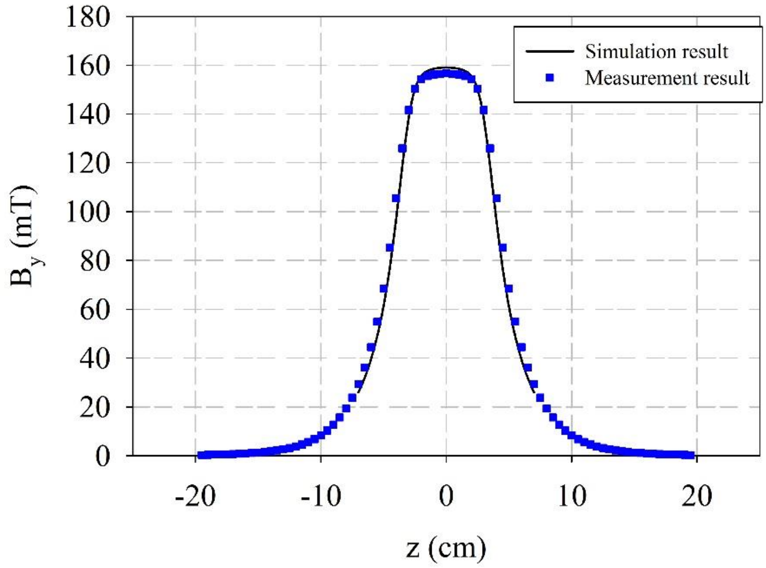

Figure 3.32: Simulated and measured magnetic field B_y distributions along the z-axis of the dipole magnet.

Both simulated and measured magnetic field distributions are similar and the field distributions in positive and negative directions of the z-axis are symmetric. The effective length of this dipole magnet is calculated by using the following equation

$$l = \frac{\int B_y dz}{B_y(0,0,0)}, \tag{3.20}$$

where $B_y(0,0,0)$ is the value of B_y at the center of the magnet. In this study, a value of integration of B_y along z-axis equals to 1678.89 mT-cm and the value of $B_y(0,0,0)$ is 156.64 mT. Therefore, the effective length of the magnet is calculated to be 10.67 cm. Normalized data of measured and simulated results are compared in Fig.3.33, which can conveniently be used in the magnetic field scaling for a certain usage.

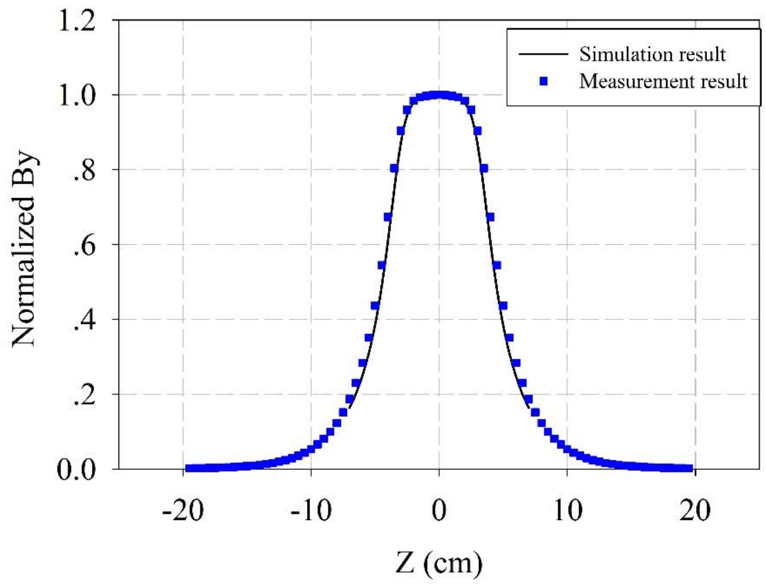

Figure 3.33: Normalized simulated and measured results of the magnetic field B_y along the z-axis of the dipole magnet.

The distribution of the normalized magnetic field B_y along the x-axis when y = 0 and z = 0 is shown in Fig. 3.34. The measurement results show that the magnitude of B_y along the x-axis almost constant within the distance of ±2 cm from the center of the magnet with the maximum variation of 0.12%. The distributions of simulated and measured magnetic field B_y along the x-axis for the distance of ±2 cm show similar tendency with small difference of about 2.58 %.

The distributions of normalized simulated and measured magnetic field B_y along the y-axis within the magnet gap of ±1 cm when x = 0 and z = 0 are shown in Fig. 3.35. Both distributions are similar and are almost constant within the distance of ±1 cm from a center of the magnet with the maximum variation of 0.1%.

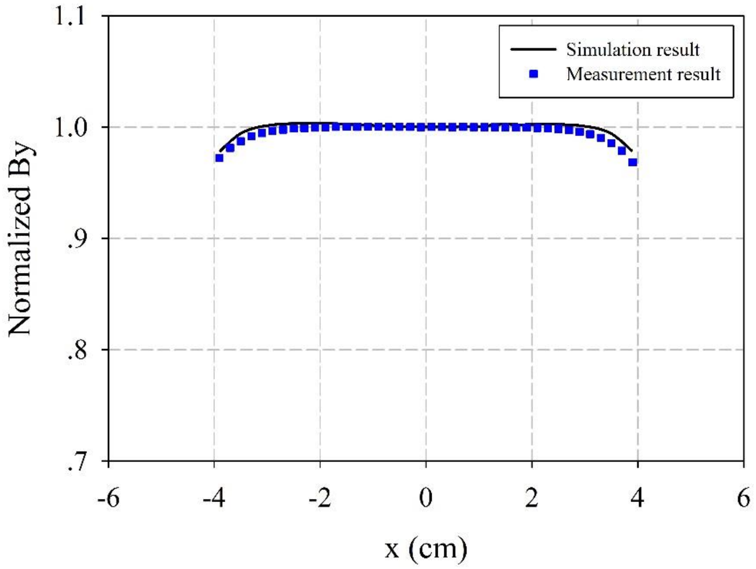

Figure 3.34: Distributions of the simulated and measured normalized magnetic field B_y along the x-axis of the dipole magnet.

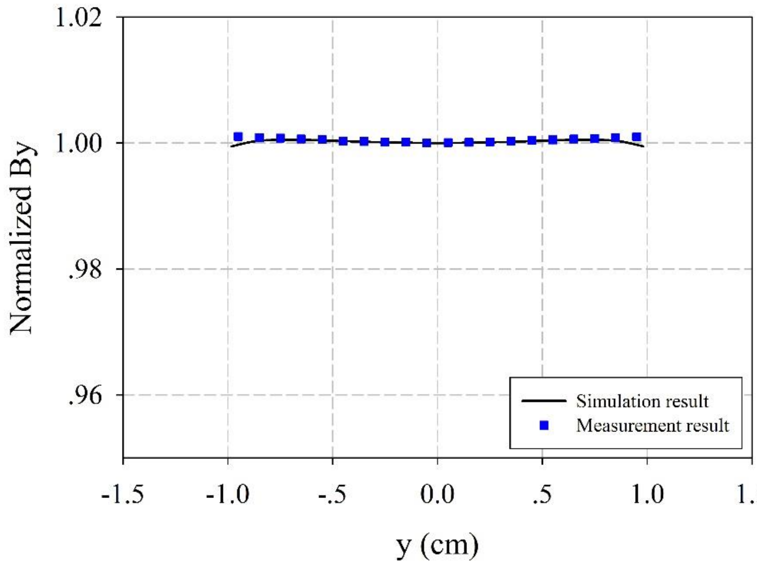

Figure 3.35: Distributions of the magnetic field B_y along the y-axis within the dipole magnet gap of ±1 cm.

The measured magnetic field B_y distribution in the x-z plane at a center of y-axis is shown in Fig. 3.36. The magnitude of B_y is almost constant at the center of the z-axis and it is around 155 mT. The center of the magnetic field is at z = 10.75 cm downstream the Mylar window exit.

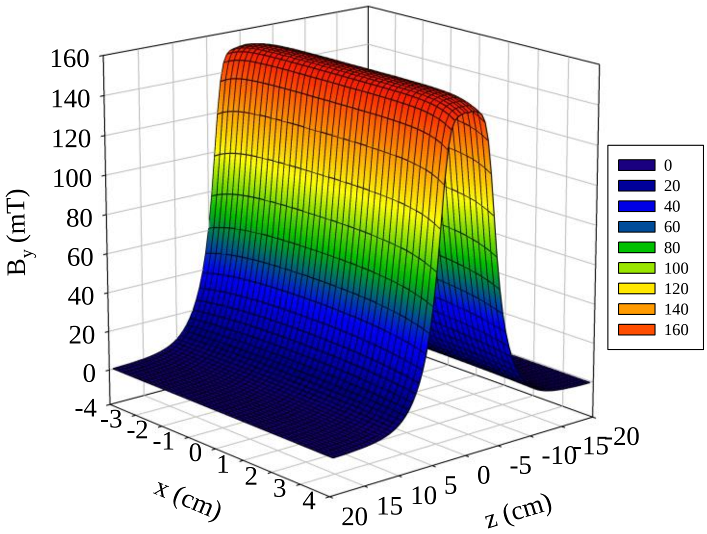

Figure 3.36: Distribution of the measured magnetic field B_y component in the x-z plane at the center of y-axis of the dipole magnet.

It is difficult to exactly determine the path length and the curvature radius of the electron trajectory along the dipole magnetic field by directly calculating from equation (3.19). This is because the magnetic field B_y is not uniform along the z-axis. Therefore, numerical calculations were conducted by including the 3-D distribution of the dipole magnetic field in PARMALA simulations.

Calculations of electron trajectories were performed by using the electrons with different energies. The electrons bend in a negative x-axis when they travel through the dipole magnetic field and hit the screen in the dispersive section. An example of histogram of the electron beam distribution in the x-axis on the screen when using the dipole magnet current of 4.5 A is shown in Fig. 3.37. Since electrons with different energies bend in the dipole magnetic field with different bending radii, they incidences on the screen at different positions. According to the dimensions of the components the experimental set-up, the center of the fluorescence screen is at x = -6 cm. In the electron beam energy measurement, a maximum beam energy is obtained by adjusting the current of the dipole magnet to have the electron beam image at the center of the screen. Then, the electron beam energies and energy distributions, which relate to the RF power and the RF phase, are calculated from the electron distribution on the screen.

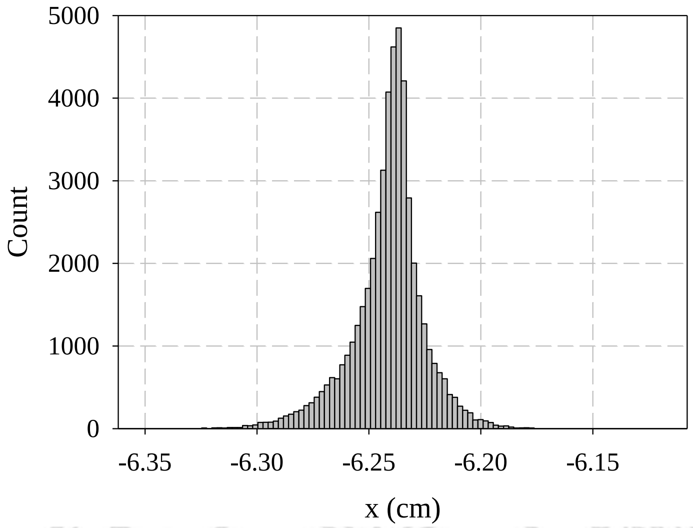

Figure 3.37: Example histogram of the electron distribution in the x-axis on the screen when the dipole magnet current of 4.5 A is used.

3.6 Measurement of Transverse Beam Emittance

In this thesis, the quadrupole scan method with a thin lens approximation was used to measure the transverse beam emittance. All related formula used to obtain the emittance value at the entrance of the quadrupole magnet are already discussed in Chapter 2. The layout of the set-up for the beam emittance measurement is presented in Fig. 3.38. The schematic diagram of the quadrupole scan method with a thin lens approximation is already shown in Fig. 2.12.

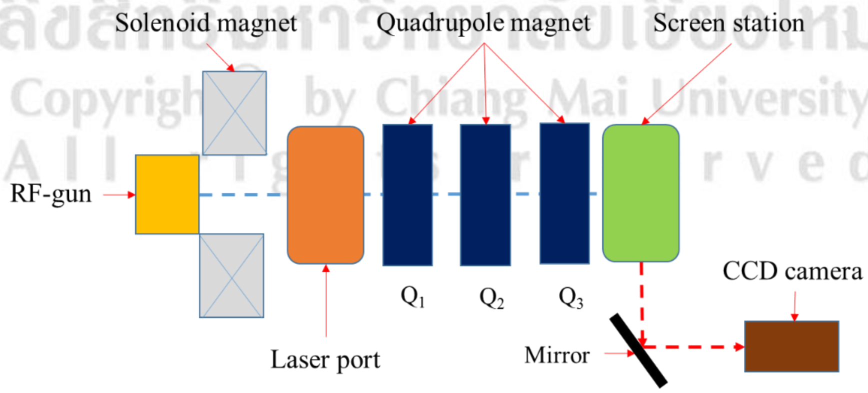

Figure 3.38: Layout of the experimental set-up to measure the beam emittance.

As shown in Fig. 3.38, there are three quadrupole magnets, used to control the transverse beam size in the accelerator system. The quadrupole magnets Q_1 and Q_3 have an effective length of 57 mm and a bore radius of 18 mm. The quadrupole magnet Q_2 has the effective length of 55 mm and the bore radius of 14 mm. In this study, the quadrupole magnet Q_3 was used in the emittance measurement. The distance from the photocathode to the center of the quadrupole magnet Q_3 is around 110 cm. During the measurements, the gradient of the quadrupole magnet is varied and the transverse beam profile on the screen is captured with CCD camera. Then, the RMS transverse beam sizes are calculated. The RMS beam size squares as a function of the quadrupole magnet focal length are plotted and fitted with the quadratic function. Lastly, the comparison of the fitting coefficients with the beam transport matrix parameters as described in Chapter 2 is performed to obtain the RMS transverse emittance value. An image of the screen used in the beam emittance measurement is shown in Fig. 3.39. The screen size is 2.5 cm in both x-axis and y-axis. The image resolution can be calculated and the resolutions of the CCD camera in x-axis and y-axis are 20.5 and 22 μm/pixel, respectively. These resolutions are used to calculate the RMS transverse beam sizes from electron distributions on the screen.

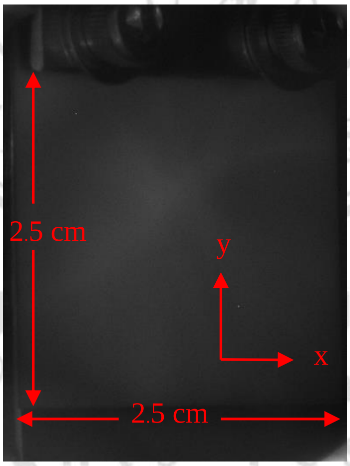

Figure 3.39: An image of the screen with dimensions used in the transverse beam emittance measurement.

The magnetic field measurements of the quadrupole magnet were performed to determine the magnetic field gradient and then used to calculated the quadrupole focal length. The set-up for the quadrupole magnetic field measurement as shown in Fig. 3.40, consists of a DC power supply, a magnetic probe, a translation state and a quadrupole magnet.

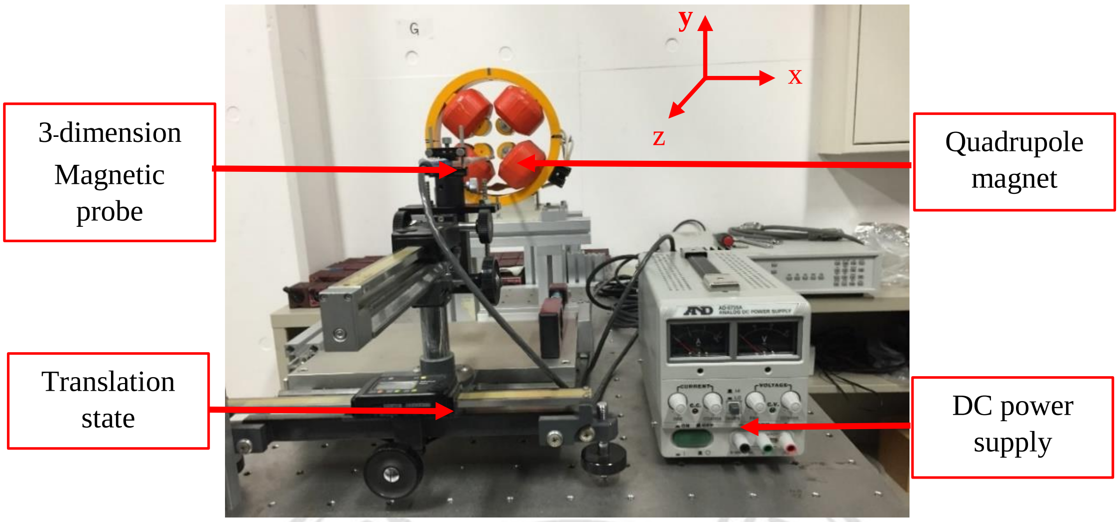

Figure 3.40: The set-up for the quadrupole magnetic field measurement.

For all measurements in this part, an electrical wire with a positive current was connected to the terminal number 1 and an electrical wire with a negative current was connected to the terminal number 4 as shown in Fig. 3.41, which leads to the magnetic field configuration in Fig. 3.42. The magnetic field was measured along the horizontal and vertical axes by using the applied currents of 0 – 2.5 A with a step of 0.5 A. Then, the gradients of the magnetic field at various positions in the gap between the magnetic poles were calculated. Finally, the effective length and the focal length of the quadrupole magnet were defined. Dimensions and properties of the quadrupole magnet used in the measurement of the transverse beam emittance are listed in Table 3.4 and the photographs of the magnet are shown in Fig. 3.43.

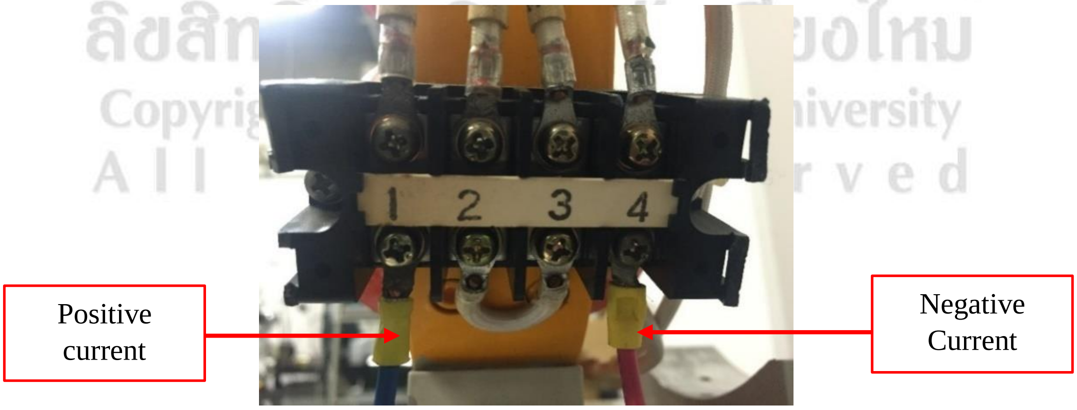

Figure 3.41: Electrical wire connection configuration of the quadrupole magnet.

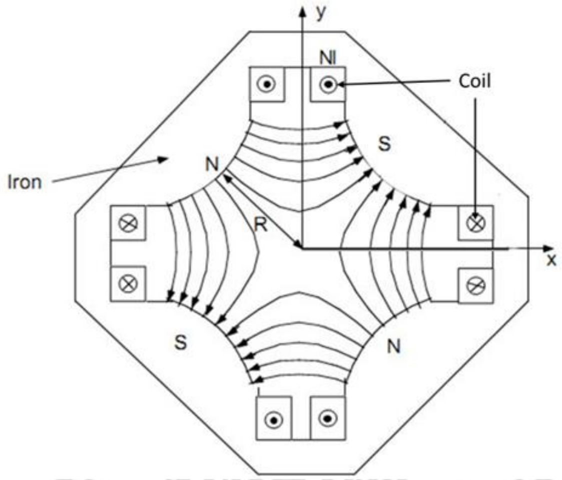

Figure 3.42: Magnetic field configuration for the measurement of quadrupole magnetic field [47].

Table 3.4: Dimensions and properties of the quadrupole magnet**.**

Property	Value
Radius aperture	34 mm
Pole face width	40 mm
Magnetic yoke width	40 mm
Magnetic yoke thickness	15 mm
Total height	210 mm
Magnetic coil size	74 mm
Number of coil turns	168 turns
Maximum applied current	6 A

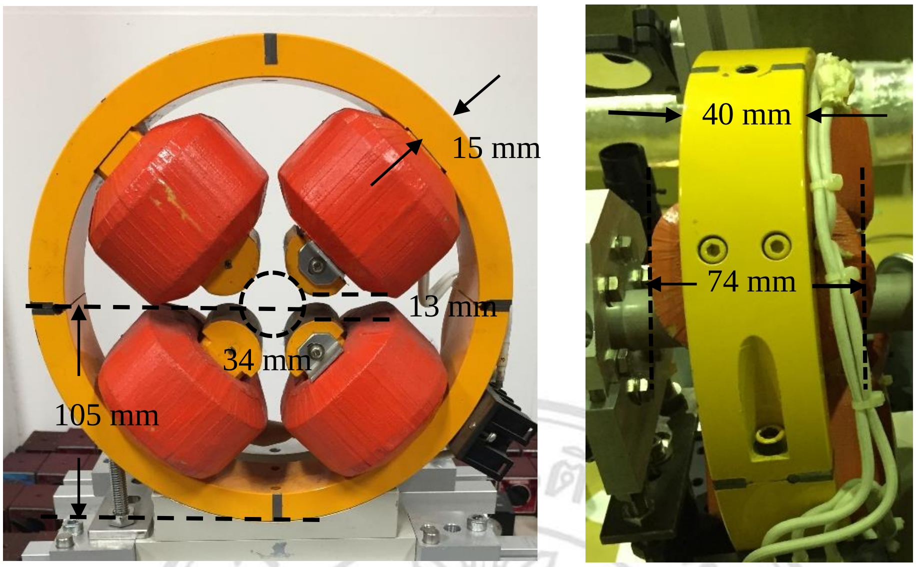

Figure 3.43: Photographs of the quadrupole magnet.

Distributions of the magnetic field along the horizontal axis (x-axis) from -46 mm to +46 mm at y = 0 mm and z = 0 mm are shown in Fig. 3.44. Distributions of the magnetic field along the vertical axis (y-axis) from -19 mm to +19 mm at x = 0 mm and z = 0 mm are shown in Fig. 3.45. Comparison between the horizontal and vertical fields (B_x and B_y) for each current shows similar tendency within the same measuring distance with the maximum difference of about 0.72% at the position (x,y) = (0,5) and (x,y) = (5, 0). As shown in Figs. 3.44 and 3.45, the magnetic field dependence on the position in x-axis and y-axis has a linear relation in the region between the four poles of the quadrupole magnet (±20 cm) and the field is zero at the center of the magnet. The magnetic field is maximum at the pole tip of the magnet.

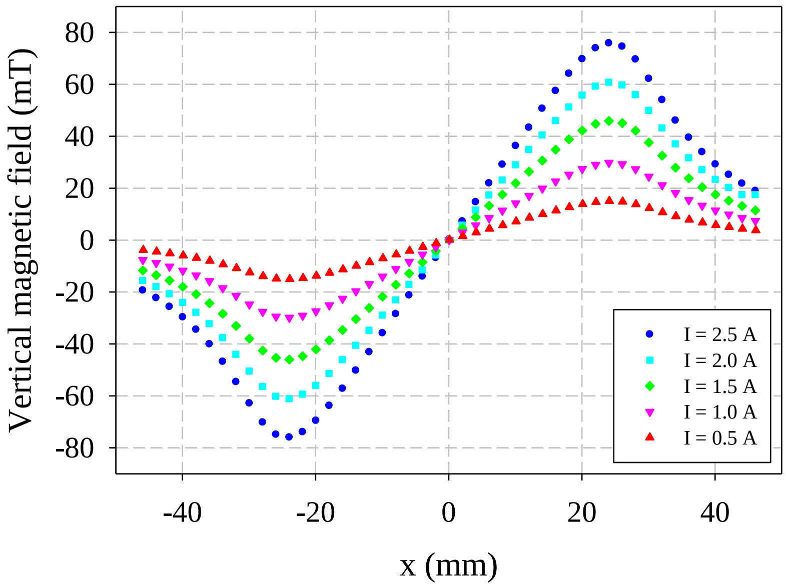

Figure 3.44: Measured vertical magnetic field as a function of the position in the x-axis.

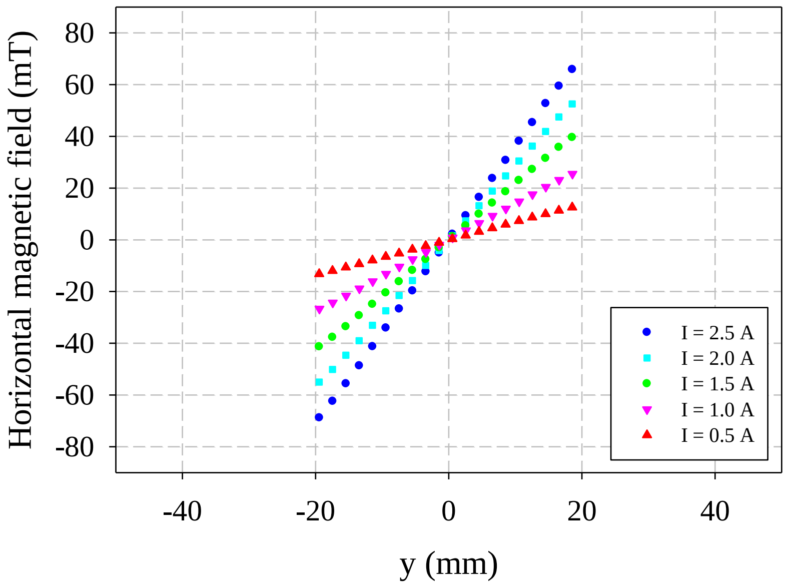

Figure 3.45: Measured horizontal magnetic field as a function of the position in the y-axis.

For the magnetic gradient estimation, the horizontal magnetic field (B_x) was measured at the position (x, y, z) = (0, 5 mm, 0) and the vertical field (B_y) was measured at the position (x, y, z) = (5 mm, 0, 0). The applied currents of 0 – 2.5 A with a step of 0.1 A were used in this measurement. Then, the gradient of the magnetic field is calculated for each current by using equations

$$g_x = \frac{B_x(y=5) - B_x(y=0)}{5} \quad \text{and} \quad g_y = \frac{B_y(x=5) - B_y(x=0)}{5}. \tag{3.21}$$

As the magnetic field depends on the applied current, the magnetic field gradient also depends on the applied current as shown in Fig. 3.46. The blue circle plots and the red square plots refer to the gradient g_x and g_y, respectively.

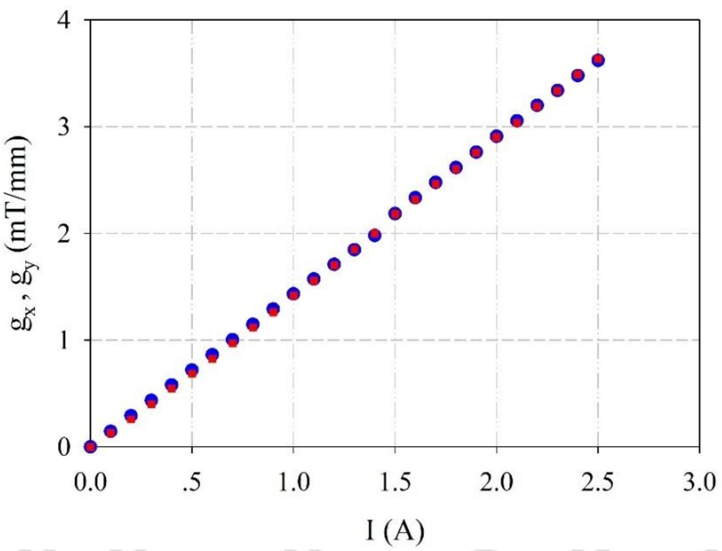

Figure 3.46: Gradients of the horizontal or vertical fields (g_x or g_y) as a function of the applied current. The blue circle plots and the red square plots refer to the gradient g_x and g_y, respectively.

The horizontal magnetic field was measured along the z-axis at the positions (x, y) = (0, 5 mm) and (x, y) = (0, 10 mm) with the applied current of 2 A. In case of the vertical magnetic field, the measured positions are (x, y) = (5 mm, 0) and (x, y) = (10 mm, 0). Then, the gradients of B_x and B_y for each position along the z-axis were calculated. Finally, the effective length of the quadrupole magnet is obtained by using the equation:

$$l = \frac{\int g dz}{\langle g \rangle}, \quad (3.22)$$

where g is the gradient of the horizontal or vertical magnetic fields (B_x or B_y) for each position along the z-axis and $\langle g \rangle$ is the average gradient of the B_x or B_y at the center of the magnet in z-axis. The distribution of the gradient g_x and an integration of g_x along the z-axis are shown in Fig. 3.47, while the distribution of the gradient g_y and an integration of g_y along the z-axis are shown in Fig. 3.48. The blue circle plots and the red square plots in both figures refer to the gradient and the integration of the gradient, respectively.

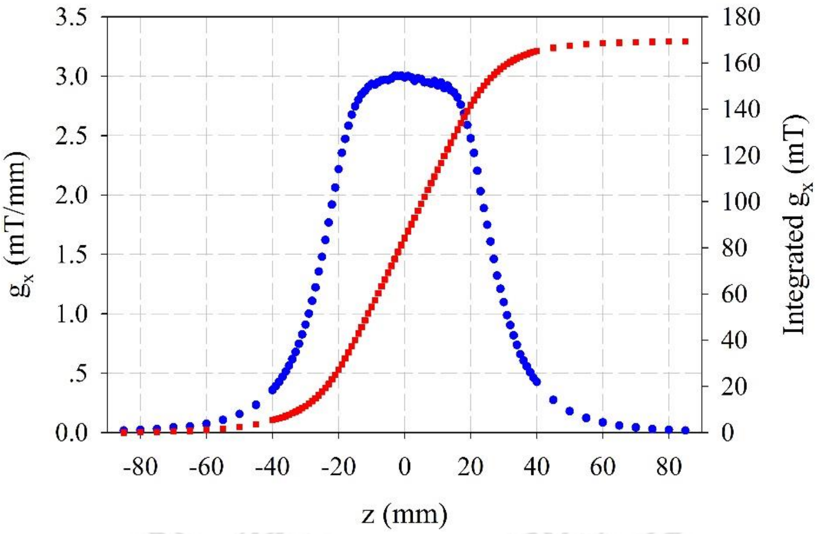

Figure 3.47: Gradient of the horizontal magnetic field (g_x) and the integration of g_x along the z-axis. The blue circles and the red squares refer to the gradient and the integration of the gradient.

The Integration of g_x along the z-axis is 169.36 mT and the average gradient is calculated to be 2.97 mT/mm. Therefore, the effective length for the horizontal field of this quadrupole magnet is 57.03 mm. Similarly, the integration of g_y along the z-axis is 167.94 mT and the average gradient is 2.95 mT/mm. Thus, the effective length for the vertical field of this quadrupole magnet is 57.03 mm.

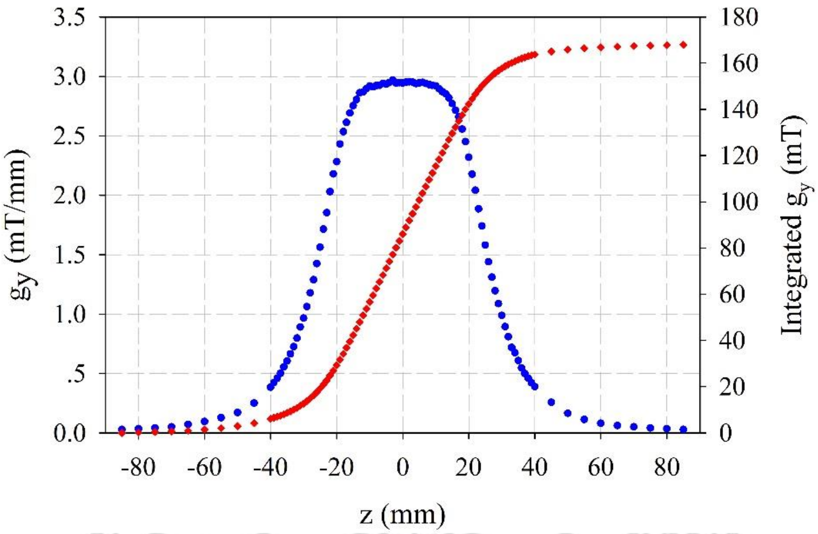

Figure 3.48: Gradient of the vertical magnetic field (g_y) and the integration g_y along the z-axis. The blue circles and the red squares refer to the gradient and the integration of the gradient.